ORIGINAL PAPER

Comparison of the Transport of Reactive Nitrogen Plasma Species into Water Bulk vs. Aerosolized Microdroplets

Mostafa Elsayed Hassan[1,2,3] · **Mário Janda**[1] · **Zdenko Machala**[1]

Abstract

This work presents the experimental study of the transport of typical air plasma long-lived reactive nitrogen species (RNS: HNO_2, NO_2, and NO) into deionized water and compares them with the most typical reactive oxygen species (ROS: H_2O_2 and O_3). RONS are generated either by external sources or by a hybrid streamer-transient spark plasma discharge, in contact with bulk water or aerosol of charged electrospray (ES) or non-charged nebulized microdroplets with a large gas/plasma-water interface. It was found that NO's contribution to NO_2^- ion formation was negligible, NO_2 contributed to about 10%, while the dominant contributor to NO_2^- ion formation in water was gaseous HNO_2. A higher transport efficiency of O_3, and a much higher formation efficiency of NO_2^- from gaseous NO_2 or HNO_2 than predicted by Henry's law was observed, compared to the transport efficiency of H_2O_2 that corresponds to the expected Henry's law solvation. The improvement of the transport/formation efficiencies by nebulized and ES microdroplets, where the surface area is significantly enhanced compared to the bulk water, is most evident for the solvation enhancement of the weakly soluble O_3. NO_2^- ion formation efficiency was strongly improved in ES microdroplets with respect to bulk water and even to nebulized microdroplets, which is likely due to the charge effect that enhanced the formation of aqueous nitrite NO_2^- ions when NO_2 or HNO_2 are transported into water. Comparisons of the molar amounts of O_3, H_2O_2, and NO_2^- formed in water by hybrid streamer-transient spark plasma discharge with those obtained with single RONS from the external sources enabled us to estimate approximate concentrations of gaseous concentrations of HNO_2, NO_2, O_3, and H_2O_2. The medium or highly soluble gaseous HNO_2 or H_2O_2, with a low concentration of <10 ppm are sufficient to induce the measured aqueous NO_2^- or H_2O_2 amounts in water. This study contributes to a deeper understanding of the transport mechanism of gaseous plasma RONS into water that can optimize the design of plasma–liquid interaction systems to produce efficient and selected aqueous RONS in water.
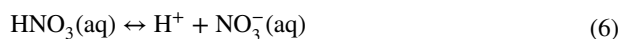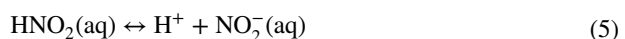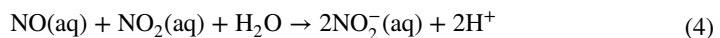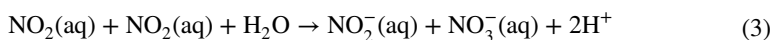
Keywords Plasma–liquid interactions · Plasma-activated water · Reactive oxygen and nitrogen species · Henry's law · Nitrous acid · Nitrogen dioxide · Nitrogen monoxide · Hydrogen peroxide · Ozone · Water electrospray · Aerosol microdroplets · Charged microdroplets · Bulk water

Extended author information available on the last page of the article

Introduction

Non-equilibrium plasma in atmospheric air produces a mixture of gaseous reactive oxygen and nitrogen species (RONS) through many electron-driven and radical reactions [1]. The primary radical species (e.g., OH, O, and N) are formed by the dissociation of air molecules. These reactive species recombine and interact with radicals/molecules to form secondary reactive oxygen and nitrogen species (ROS and RNS, collectively RONS). ROS include hydrogen peroxide (H_2O_2) and ozone (O_3), while RNS include nitrogen monoxide (NO), nitrogen dioxide (NO_2), as well as nitrous (HNO_2) and nitric (HNO_3) acids [2, 3]. HNO_2 and HNO_3 are dominantly formed via OH radicals in the three body reactions (1) and (2), respectively [4, 5].

$$NO + OH + M\left(= O_2 \text{or } N_2 \right) \rightarrow HNO_2 + M \tag{1}$$

$$NO_2 + OH + M \rightarrow HNO_3 + M \tag{2}$$
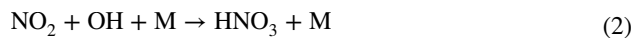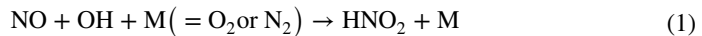
In plasma discharges interacting with water, these gaseous plasma RONS are transported through the plasma–water interface into water, inducing the production of so-called "plasma-activated water" (PAW). Many applications of PAW have been documented [6–9]. A large area of application is in medicine and bio-decontamination, where PAW solutions are effective in killing microbes in suspension or biofilms on surfaces [10–14]. Some PAW solutions have shown anticancer effects and represent a novel cancer therapeutic strategy [15–17]. In the food and agricultural research, PAW promotes seed germination [18, 19], improves plant growth [20–22], and prevents plant diseases and food spoilage [23, 24]. In environmental science applications, PAW can be used in water cleaning as a promising approach for micropollutant decontamination and causes antibacterial properties of water [22, 25, 26]. The composition of plasma RONS and their distribution in the gas and liquid phases depends on multiple parameters, such as the type of plasma discharge, the configuration of the discharge reactor, discharge characteristics (e.g. frequency, voltage, current, and power), the composition of the working gas and its flow rate, and the liquid (activated by the plasma discharge), which in turn affect the final composition of PAW [27–35]. The solvated aqueous RONS in PAW include long-lived reactive species such as H_2O_2, O_3, and nitrite (NO_2^-) and nitrate (NO_3^-) anions, as well as many other short-lived species [36–38]. Nitrogen oxides (NOx) and nitrous and nitric acids (H)NOx formed in plasma dissolve in water and dissociate into NO_2^- and NO_3^- aqueous anions. Protons (H^+) are inevitably released when these anions are formed in the PAW, typically making acidic pH of the PAW via the following reactions (3–6) [39–41].

$$NO_2(aq) + NO_2(aq) + H_2O \rightarrow NO_2^-(aq) + NO_3^-(aq) + 2H^+ \tag{3}$$

$$NO(aq) + NO_2(aq) + H_2O \rightarrow 2NO_2^-(aq) + 2H^+ \tag{4}$$

$$HNO_2(aq) \leftrightarrow H^+ + NO_2^-(aq) \tag{5}$$

$$HNO_3(aq) \leftrightarrow H^+ + NO_3^-(aq) \tag{6}$$

The solubility of the gaseous RONS in water varies markedly, and even if their concentrations in the gas phase are similar, their achieved aqueous concentrations in water

are significantly different due to very different Henry's law solubility coefficients of each gaseous species [42]. Table 1 shows Henry's law solubility coefficients k_H (mol/m^3 Pa), under the equilibrium conditions, for the most typical gaseous plasma RONS. Henry's law describes the proportionality of the aqueous phase concentration of species to its equilibrium partial pressure in the gas phase. Henry's law coefficient can be also expressed as the dimensionless ratio between the aqueous phase concentration of species to its gas phase concentration as k_H^{cc} [43, 44].

Due to the significantly different k_H^{cc} for each gaseous RONS generated by plasma in air (gas phase), these species dissolved in water reach very different aqueous concentrations. While the highly soluble species such as H_2O_2 is readily transferred into the water, the weakly soluble species, such as NO_2, NO, and O_3, are hardly dissolved into water as NOx$^-$ and O_3(aq), respectively [45]. In recent years, plasma RONS formation in plasma-liquid systems has been studied mainly by numerical simulations and a few experimental studies [46–51]. Gorbanev et al. [52] and Winter et al. [53] assessed the transition of H_2O_2 into the liquid and found a direct correlation between the concentration of H_2O_2 in the gas phase and the liquid media. Oinuma et al. [54] studied the near-interfacial reactions of controlled-size microdroplets with plasma generated OH radicals and the related transport of H_2O_2. Machala et al. [55] observed the formation of RONS by two types of atmospheric air plasma discharges in contact with water, streamer corona (SC) and transient spark (TS). SC discharge was characterized by low power (0.2–0.4 W), short low current pulses (~ 10 mA, 10–100 ns), and with a typical repetition frequency of 10–30 kHz, while TS was characterized by higher power (1.5–2.3 W), short high current pulses (~ 10 A, ~ 25 ns), and with a typical repetition frequency of 1–4 kHz [56]. SC resulted in the dominant formation of H_2O_2 and O_3, and TS resulted in H_2O_2 and (H)NOx. The produced gaseous RONS are readily dissolved in water resulting in aqueous H_2O_2(aq), O_3(aq), NO_2^-, and NO_3^-, respectively, in the PAW.

One of the ways to prepare the PAW efficiently is by improving the RONS transfer into water by increasing the total water surface area using the water aerosolization process by producing water microdroplets of a high surface-area-to-volume ratio [49]. This significantly increases the plasma–water interaction surface area and thus enables more efficient transfer of the plasma reactive species into the water, which is of vital importance, especially for the badly soluble species, such as NO, NO_2, and O_3. Although aerosolization in some experimental arrangements reduced the RONS concentrations in PAW [57], the approach of increasing plasma–liquid interaction surface area in microdroplets was adopted by several research groups [14, 54, 58–62]. Janda et al. [63] generated TS coupled with the formation of water microdroplets, which increased the plasma-water interaction surface area, and thus the higher transfer of weakly soluble gaseous species such as NO_2 into water can be achieved. Stancampiano et al. [64] concluded in their review that aerosol droplets in contact with plasma act as efficient microreactors, which will lead to opening

Table 1 Henry's law solubility coefficients k_H and k_H^{cc} of gaseous species [44]

Gaseous species	k_H (mol/m^3 Pa)	k_H^{cc}
H_2O_2	9.1×10^2	2.26×10^6
HNO_2	4.8×10^{-1}	1.19×10^3
NO_2	1.2×10^{-4}	2.97×10^{-1}
NO	1.9×10^{-5}	4.71×10^{-2}
O_3	10^{-4}	2.48×10^{-1}

new horizons for future applications of plasma–aerosol e.g., for the *in-situ* delivery and transport of chemicals into the liquid droplet.

This experimental work is focused on studying the transport mechanism of medium vs. weakly soluble gaseous RNS namely: HNO_2, NO_2, and NO generated in the atmospheric air by either external sources or by streamer corona discharge in contact with water in hybrid gas/plasma–bulk/aerosol interaction systems in different configurations. The formation of aqueous RONS was also investigated in a hybrid streamer-spark discharge system using nebulized and electrospray microdroplets. This work follows our previously published works where the transport mechanism of high and low soluble ROS (H_2O_2 and O_3) in bulk water and electrosprayed (ES) microdroplets were studied [65], and the optical diagnostic techniques were used to analyze the size, surface area, velocity, and lifetime of the ES water microdroplets [66].

The novelty of this work is in providing a deeper insight into the plasma RONS transport into the water as a function of different key parameters such as interaction time, gas–water (interface and surface area), and the effects of charged vs. non-charged microdroplets. Our findings will lead to a better fundamental understanding of the plasma–water interaction and transport chemistry which can be employed in many air plasma-liquid systems and their applications.

Experimental Setup

Low-temperature plasma in humid air produces several types of reactive species, most of which are soluble in water. In addition to the "gas–liquid transport" (solvation) of species, chemical reactions between these species occur in both the gas and water phases. Generating a mixture of reactive species by plasma directly in a reactor, where they also dissolve in water, can make it difficult to study the solubility of individual reactive species. To avoid the influence of chemical interactions, we perform experiments to study the solubility of individual gas species, NO, NO_2, HNO_2, O_3, and H_2O_2, entering the reactor from external sources.

In this section, we first describe the external sources used to generate the single gas species. Then, we describe the reactors for solvation of the studied species in bulk water, water microdroplets generated by electrostatic spraying, and nebulized microdroplets. Then, we describe the experimental apparatus where plasma directly interacts with water microdroplets. In the last subsection, we describe the diagnostic tools used.

Experiments with gas species from external sources

The external sources of gas species

The working gas (ambient air) with a concentration of 100 ppm H_2O_2 was obtained by bubbling air through a 30% w/w H_2O_2 solution. The gas flow rate in the experiments with H_2O_2 was 2 L per minute.

The external O_3 source was a commercial dielectric barrier discharge generator (Easelec E03G). The gas at the outlet of the ozone generator was mixed with ambient air to give an O_3 concentration of approximately 450 ppm. The total gas flow rate through the reactor for the experiments with O_3 was 0.8 L per minute.

Gaseous HNO_2 was obtained by pumping ambient air at a flow rate of 1 L per minute through a bubbler with a solution obtained by mixing aqueous solutions of $NaNO_2$ and HCl, each at a molar concentration of 50 mM, yielding 20 mM HNO_2 solution. In addition to HNO2, the gas mixture produced by bubbling this aqueous mixture also contained NO and NO_2. The concentration of these species in the bubbled gas gradually decreased over time. The initial decrease in the concentration was rapid but gradually slowed down. After about 6 min, the decrease was very slow, resulting in almost constant concentrations of HNO_2, NO, and NO_2 in the gas. Only then did the bubbled gas enter the reactor so that the average concentration of HNO_2, NO_2, and NO during the 1–4 min solvation experiments was approximately 100, 250, and 600 ppm, respectively.

A calibration cylinder containing 2000 ppm NO in N_2 was used as a source of pure external NO. This mixture was diluted with molecular nitrogen (99.999% purity) to a working concentration of 600 ppm NO at a total gas flow rate of 1 L per minute.

A calibration cylinder containing 1000 ppm of NO_2 in synthetic air (80% N_2, 20% O_2) was used as an external source of NO_2. The NO_2 concentration was reduced to 250 ppm by mixing with ambient air at a total gas flow rate of 1 L per minute. The gas flow rate was adjusted in all experiments using Aalborg flow meters.

Concentrations of 600 and 250 ppm of NO and NO_2, respectively, were chosen because such concentrations of NO and NO_2 were present in the experiments with the gas mixture containing HNO_2 in air. In addition, similar concentrations of NO and NO_2 are generated in air by transient spark discharge, which has been studied in our group [63].

Gas species of H_2O_2, HNO_2, NO_2, NO, and O_3 from external sources, were studied individually (not mixed with each other), with the specific flow rates and gas concentrations as shown in Table 2.

Although in most of the experiments with NO or NO_2 from the calibration pressure cylinders, only one of these two nitrogen oxides (either NO with concentration of 600 ppm or NO_2 with concentration of 250 ppm) was in the working gas, we also performed a special experiment with bulk water only, in which we used a mixture with 600 ppm of $NO + 100$ ppm of NO_2.

Table 2 List of the gas mixtures used in experiments focused on solvation of single gas species provided by the external sources

Species in inlet gas	Concentration [ppm]	Gas flow rate [l/min]	Description
H_2O_2	100	2	Air bubbled through H_2O_2 water solution
O_3	450	0.8	Outlet from an ozone generator diluted with the air
NO	600	1	Cylinders (2000 ppm of NO in N_2, diluted with additional N_2)
NO_2	250	1	Cylinder (1000 ppm of NO_2 in synthetic air, diluted with ambient air)
NO	600	1	Cylinders (2000 ppm of NO in N_2, diluted with additional
NO_2	100		$N_2 + 1000$ ppm of NO_2 in synthetic air, diluted with ambient air). Only in bulk water experiments
HNO_2	100	1	Air bubbled through a 20 mM solution of HNO_2 prepared
NO	600		by mixing 50 mM solutions of $NaNO_2$ and HCl in water
NO_2	250		

Bulk water setup

Figure 1 shows a schematic of the experimental setup for the study of gaseous species transport in bulk water. The setup consists of the external gas sources (described in the previous subsection), a gas chamber, a bulk water reactor, and the gas phase analytical techniques (described in subSect. "Gas Diagnostics").

The bulk water reactor and the gas chamber have a cylindrical geometry with a diameter of 13 mm. The height of the gas chamber is 11 mm, and the internal volume is ~1.4 ml, the same as the gas phase volume in the bulk water reactor. The water volume in the bulk water reactor was varied from 200 μl to 1000 μl. The water volume changes were enabled by a piston at the bottom of the bulk water reactor. The change in the water volume changed the height of the water depth, whereas the surface area of water was constant. The bulk water surface area exposed to the gaseous species was approximately 133 mm^2.

The gas chamber is used to bypass the bulk water reactor before a stable working gas mixture is reached. When a desired initial concentration of gas species was reached, a 3-way solenoid valve (TP-DD014S040F-012DC) diverted the gas flow into the bulk water reactor filled with the specified volume of water. The duration of the treatment time during which the bulk water was exposed to the incoming gas species was 1, 2, or 4 min. At the end of the treatment time, the gas flow was diverted back to the gas chamber by the 3-way solenoid valve.

Electrospray microdroplets setup

Figure 2 shows a schematic of the experimental setup for the investigation of the gaseous species transport into charged electrospray water microdroplets. The setup consists of the external gas sources (described in subSect. "The external sources of gas species"), a reactor, a water supply unit, a DC high voltage (HV) power supply, electrical diagnostic tools, and gas phase analytical techniques (described in subSect. "Gas Diagnostics").
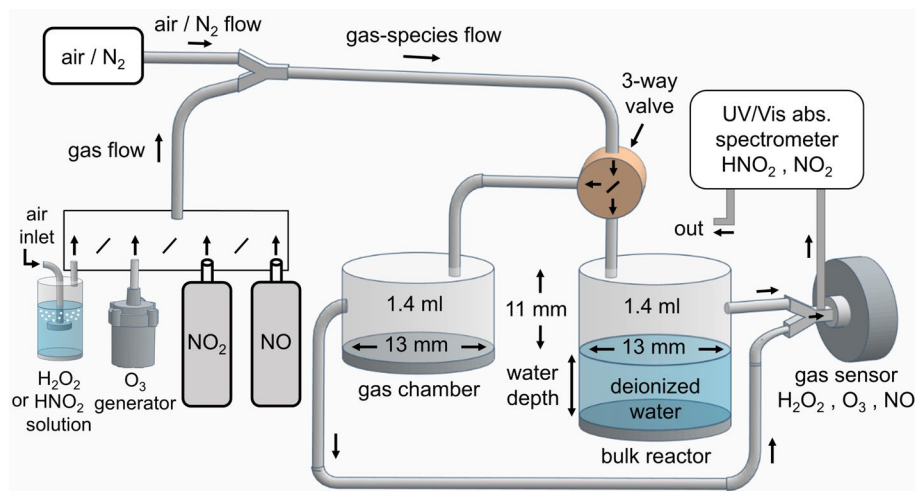

Fig. 1 Schematic of the experimental setup for investigation of the gaseous species transport into bulk water
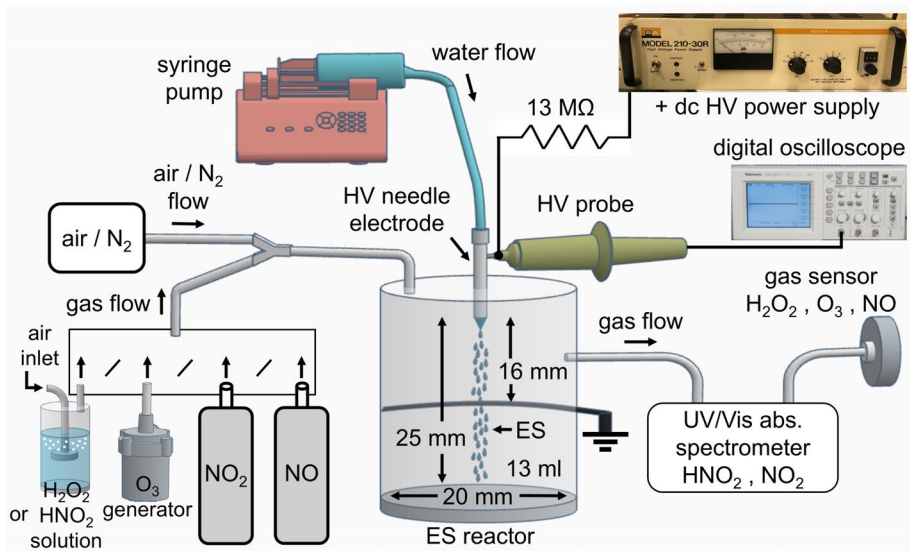
Fig. 2 Schematic of the experimental setup for the investigation of the gas species transport into electrospray (ES) water microdroplets

To generate an electrospray of water microdroplets, a syringe pump (NE-300) continuously delivers deionized water to the reactor through a blunt hollow stainless steel needle (nozzle) with an inner diameter of 0.5 mm and an outer diameter of 0.7 mm. The needle, acting as the anode, is connected to an HV power supply (Spellman Bertan 210-30R) via a 13 MΩ ballast resistor. The applied voltage is monitored using a DC HV probe (Agilent N2771A) and the signal is processed by a digital oscilloscope (Tektronix TDS 1012).

The applied high voltage of positive polarity must exceed 5 kV to generate a sufficiently strong electric field between the tip of the needle (anode) and the grounded wire electrode (cathode) to form the electrospray of charged water microdroplets. The gap between the two electrodes is 16 mm, and the diameter of the grounded stainless steel wire electrode is 1.5 mm. Both electrodes are enclosed in a transparent cylindrical plastic reactor with a diameter of 20 mm and a height of 41 mm.

The syringe pump and the HV power supply are turned on for two minutes once the concentration of gas species in the working gas mixture has reached and stabilized at the desired value. The water flow rate in the experiments ranged from 200 to 1000 µl/min, and the applied voltage varied between 5 and 13 kV.

The average size of ES microdroplets generally decreases with increasing applied voltage. The ES microdroplets are not uniform in diameter but are characterized by a polydisperse distribution of diameters (5–400 µm). For each applied voltage and water flow rate, we previously measured histograms of the polydisperse distribution of ES microdroplets diameters [65, 66] and this data was used here.

The water microdroplets gradually accumulated and formed a bulk water at the bottom of the reactor below the grounded electrode. With the experiment duration of 2 min, the total amount of water collected inside the reactor was up to 2 ml (at the water flow rate of 1000 µl/min). Therefore, there is an adjustable piston at the bottom of the reactor to keep the average volume of the gas space above the water level constant at 13 ml, regardless

of the water flow rate and the final volume of the water collected inside the reactor. It is necessary to keep the gas space constant so that the average residence time of the gas inside the reactor does not decrease with the increasing water flow rate.

Nebulized microdroplets setup

Figure 3 shows a schematic diagram of the experimental setup for the investigation of the gas species transport to non-charged nebulized microdroplets. The setup consists of the external gas sources (described in subSect. "The external sources of gas species"), a reactor, a water supply unit (nebulizer), an ice bath, and the gas phase analytical techniques (described in subSect. "Gas Diagnostics"). Unlike in the previous setups, the gas composition is monitored before entering the reactor.

     The nebulizer reactor has a cylindrical geometry with a diameter of 27 mm. The height of the reactor is 90 mm and the internal volume is 50 ml. The nebulizer (Omron NE-C300-E) mechanically produces a mist of nebulized water microdroplets with a monodisperse size distribution of approximately 1 μm in diameter. The nebulizer delivers 500 μl of water in the form of microdroplets to the reactor every minute.

     The experiment starts, i.e. the nebulizer is turned on for four minutes, only when the concentration of gas species in the working gas mixture reaches the desired stable value. Unlike the ES microdroplets, the nebulized microdroplets do not form bulk liquid water at the bottom of the reactor. Some of the nebulized microdroplets are deposited on the walls of the reactor, but most are carried out of the reactor by the flowing gas mixture. To collect the water sample for further analysis, an ice bath was used to enhance the condensation of the aerosol mist. However, only 200–500 μl of water accumulated in a silicon tube immersed in the ice bath after the 4-min experiment that could be collected.

Plasma-water interaction setup

Figure 4 shows a schematic of the experimental setup for studying the species transport from plasma into water. The setup consists of a water supply unit, an air pump, a reactor,
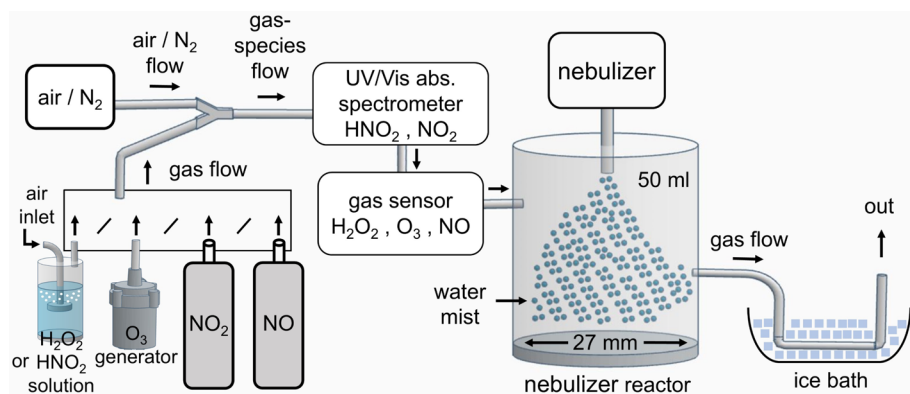

Fig. 3 Schematic of the experimental setup for the study of gas species transport into non-charged nebulized microdroplets
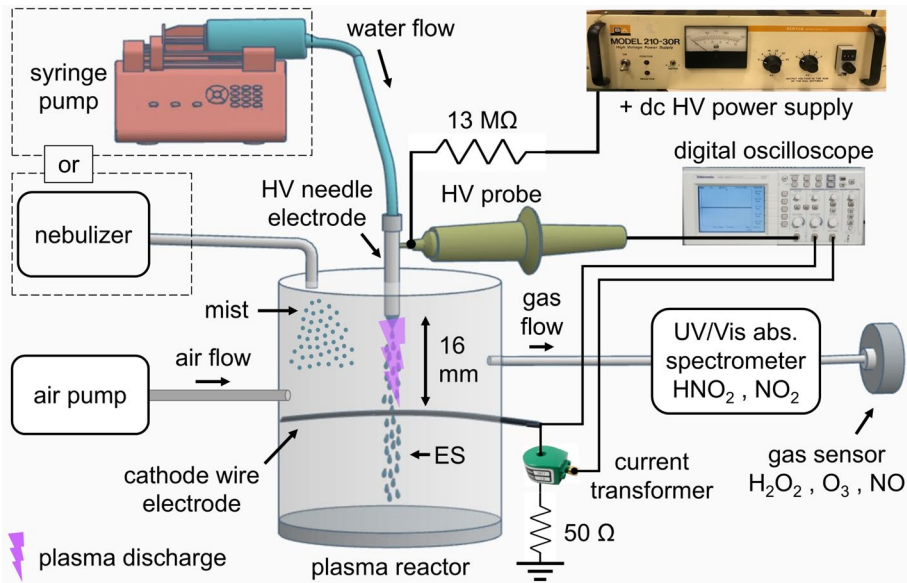
Fig. 4 Schematic of the experimental setup for studying the transport of plasma-generated species into water. Both water supply units were utilized: either the syringe pump with water flow through the needle electrode or the nebulizer

a DC HV power supply, electrical diagnostic tools, and gas-phase analytical techniques (described in subSect. "Gas Diagnostics").

A blunt needle (as HV electrode) with outer and inner diameters of 0.7 and 0.5 mm is used as the anode, which enters the reactor from the top. The needle electrode is connected to the HV power supply (Spellman Bertan 210-30R) through a ballast resistor with a resistance of 13 MΩ. The applied voltage is measured by an HV probe (North Star PVM-12, bandwidth 80 MHz). The current is measured as a voltage drop across a 50 Ω resistor shunt connected between the ground and the cathode (a 1.5 mm diameter stainless steel wire) or by a current transformer (Pearson Electronics model 2877). All electrical signals are processed by a digital oscilloscope (Tektronix TDS 2024).

The measured electrical signals are used to calculate the discharge power (P) and input energy density (E) [67]. The discharge power of pulsed discharges can be calculated from the measured voltage (V) and current (I) waveforms using Eq. (7):

$$P = f \times \int_T (V \times I) dt \tag{7}$$

where T is the period covering the entire current pulse and f is the frequency of the discharge current pulses. The input energy density in [J/l] can be calculated using Eq. (8):

$$E = 60 \times P/q \tag{8}$$

where q is the input gas flow rate in [l/min].

Unlike previous setups, the reactive species are formed directly inside the reactor by the plasma discharge generated in contact with water aerosol at 16 kV (15 kV at the HV needle electrode) supplied by the HV power supply between two stainless steel electrodes with a gap of 16 mm in ambient air pumped into the reactor at a flow rate of 1 l/min.

Two different plasma reactors are used depending on the water aerosol system used. Plasma and charged ES water microdroplets are produced simultaneously in the reactor described in subSect. "Electrospray microdroplets setup". To study the interaction of the plasma with the mist of non-charged nebulized microdroplets, electrodes were installed in the nebulizer reactor described in subSect. "Nebulized microdroplets setup".

Diagnostics Tools

Gas Diagnostics

The UV–Vis absorption spectroscopy was used to monitor NO_2 and HNO_2 in the working gas. A pulsed Xe lamp (Ocean Insight PX-2) was used as the light source and absorption spectra were measured with an optical emission spectrometer (Ocean Insight STS-UV). The spectral resolution of this spectrometer is 3 nm, and the spectra were recorded in the range of 185–665 nm. An absorption path length of 32 cm was achieved by using a mirror to make a double pass through a 16 cm cuvette. The concentrations of NO_2 and HNO_2 could be detected in the range from 20 to more than 1000 ppm.

The UV–Vis absorption technique is absolute. The concentrations of NO_2 and HNO_2 in the gas were obtained by fitting the measured spectra with calculated 'synthetic' spectra. The synthetic UV–Vis absorption spectra were calculated from the absorption cross sections for NO_2, and HNO_2 downloaded from the MPI-Mainz UV/VIS spectral atlas [68]. These absorption cross sections were convoluted to match the spectral resolution of our spectrometer, while keeping the area under the curve constant. This approach was verified by measuring the NO_2 concentration in a calibration gas mixture from a cylinder with 1000 ppm of NO_2.

Electrochemical gas sensors (Membrapor) with a full-scale output of 20 mA (200 mV) were used for the detection of H_2O_2, O_3, and NO. The H_2O_2 gas sensor (H2O2/CB-500) has a nominal range of 0–500 ppm, a resolution of < 1 ppm, a maximum overload of 1000 ppm, and an output signal of 200 ± 50 nA/ppm. The O_3 gas sensor (O3/C-1000) has a nominal range of 0–1000 ppm, a resolution of 0.3 ppm, a maximum overload of 2000 ppm, and an output signal of 170 ± 30 nA/ppm. The NO gas sensor (NO/SF-1000) has a nominal range of 0–1000 ppm, a resolution of 0.5 ppm, a maximum overload of 2500 ppm, and an output signal of 200 ± 50 nA/ppm. Each gas sensor was attached to a transmitter board connected to an Arduino circuit. The Arduino circuit processed the signals from the sensors and displayed the concentrations of H_2O_2, O_3, and NO on an attached LCD display. The gas sensors and UV–Vis absorption cell are connected to the reactor with polytetrafluoroethylene flexible PTFE (Teflon) and silicone tubing.

Water diagnostics

The pH of the liquid samples was measured with a pH probe (WTW SenTix Mic) using a pH meter (WTW pH 3110). The pH of the deionized water (with conductivity < 3 μS/cm) before the treatment was 5.2. The UV–Vis spectroscopic colorimetric methods are used for the chemical analysis to measure the concentrations of the dissolved species in water in the aqueous phase. The collected water samples with added chemical reagents (after less than 1 min from the end of the experiment) are analyzed by a UV/VIS absorption spectrophotometer UV-1800 Shimadzu.

For H_2O_2(aq) and O_3(aq), reagents of Titanium oxysulfate ($TiOSO_4$) and indigo blue II are used [69–71], respectively, as described in [65]. For the analysis of NO_2^-, Griess reagent is used that reacts with NO_2^- under acidic conditions and converts into a deep purple azo compound. Colorimetric Assay Kits #780,018 and 780,020 contain the prepared ready-to-use Griess reagents: R1 and R2, respectively, provided by Cayman Chemicals, to detect the concentration of NO_2^- from 2 up to 50 μM, as calibrated in our laboratory. The NO_2^- sample is prepared as (sample: R1: R2 = 2: 1: 1), then after 10 min of mixing, the maximum absorption is measured at 540 nm.

Results and Discussion

Transport of species from external sources into bulk water

Figure 5 shows the amount of NO_2^- ions formed in 200–1000 μl of water during 1–4 min experiments (static water surface area of bulk water experiment) with external sources of species. The working gas contained either 600 ppm of NO in N_2 (Fig. 5a) or 250 ppm of NO_2 in synthetic air (Fig. 5b).

Despite lower gas phase concentrations, NO_2 gas produces roughly six times more NO_2^- ions in bulk water than NO gas. To better compare the contributions of NO and NO_2 to the NO_2^- ion formation, we introduce a new metric: NO_2^- formation efficiency. This is defined as the ratio of NO_2^- ions formed in water to the total number of NO_2 or NO molecules initially present in the gas phase.

NO_2^- ion formation in water from nitrogen oxides (NO and NO_2) involves their dissolution (governed by Henry's law constants in Table 1) followed by the aqueous reactions (3–4) which were described earlier. In the presence of NO_2 gas (Fig. 5b), only reaction (3) is relevant. However, when only NO gas is introduced, reaction (4) necessitates the presence of NO_2, which can form from the oxidation of NO by trace amounts of air in the system. Despite using a NO/N_2 gas mixture, we cannot exclude the possibility of NO converting to NO_2 due to minor air leaks or surface reactions within the apparatus.
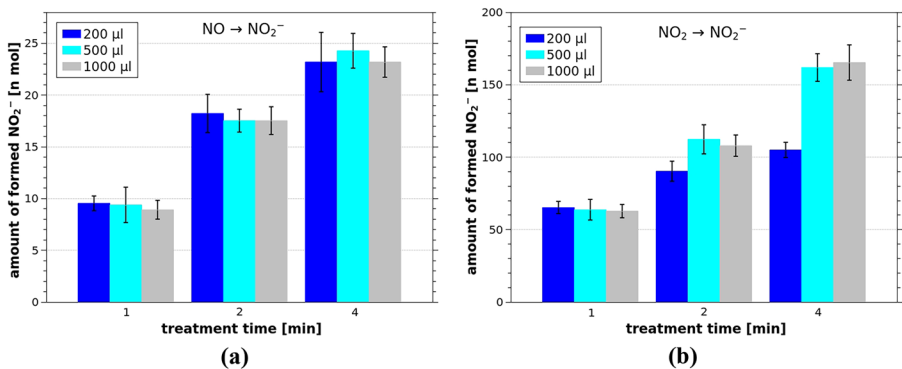

Fig. 5 Molar amounts of NO_2^- ions formed in bulk water as a function of treatment time and water volume, under constant water surface area, with the following inlet gas conditions: (**a**) 600 ppm of NO in N_2; (**b**) 250 ppm of NO_2 in synthetic air

To clarify the relative contributions of NO and NO_2 to the NO_2^- ion formation in water, we conducted an experiment with mixtures of NO (600 ppm) and NO_2 (100 ppm). We calculated the NO_2^- formation efficiency using only the NO_2 concentrations (100 ppm). The results of this experiment revealed that the efficiency of the NO_2^- formation from NO_2 alone was statistically indistinguishable from that in the NO/NO_2 mixtures. This finding strongly suggests that the direct contribution of NO to NO_2^- formation is negligible and thus will not be considered further (explained in the Supplementary Material in more detail). The conversion of NO into NO_2 would be an important step to enhance the NO_2^- ion formation, but it disables us from reliably studying the sole direct contribution of NO to the NO_2^- formation, since the results from the experiments using NO/N_2 mixtures may be significantly affected by partial unavoidable conversion of NO to NO_2.

Neglecting the influence of NO also simplified the analysis of results from the measurements in the $NO/NO_2/HNO_2$ (HyNOx) mixtures, allowing us to focus on the relative contributions of HNO_2 and NO_2 to the NO_2^- ion formation. Gaseous HNO_2 contributes to NO_2^- ion formation via efficient dissolution in water (with Henry's law coefficient approximately 4000 times greater than that of NO_2) followed by its direct dissociation in water (reaction 5).

Figure 6 shows the amount of NO_2^- detected in 200–1000 μl of water after experiments of 1–4 min treatment time with the H_yNO_x gas mixture (~600 ppm of NO, ~250 ppm of NO_2, and ~100 ppm of HNO_2). The amount of NO_2^- ions formed in water is about 1 order of magnitude higher than in the experiment with only 250 ppm of NO_2 from the pressure cylinder without HNO_2 (Fig. 5b). These results show that HNO_2 plays a dominant role in the formation of NO_2^- ions. Based on these results we can estimate that less than 10% of NO_2^- ions are formed by the solvation of NO_2 molecules via reactions (3–4).

Figure 6 presents not only the total amount of NO_2^- ions formed in the water but also the amount of NO_2^- remaining after subtracting the expected NO_2^- formed from 250 ppm of NO_2 gas alone (based on data from Fig. 5b). We assume that the reduced amount of
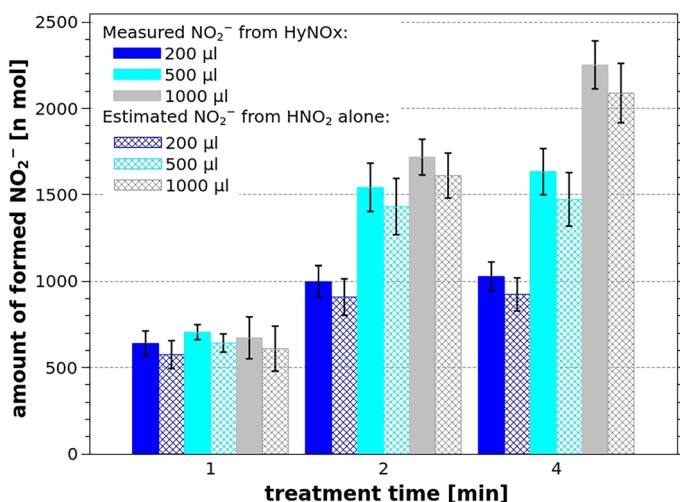

Fig. 6 Molar amounts of NO_2^- ions formed in the bulk water in the experiment with HyNOx mixture (~600 ppm of NO, ~250 ppm of NO_2, and ~100 ppm of HNO_2). Solid bars represent the measured amount of NO_2^- ions, while hatched bars indicate the estimated contribution from HNO_2 alone

NO_2^- ions (without accounting for NO_2 gas) comes from the direct solvation of HNO_2 (reaction 5). By utilizing this reduced amount of NO_2^- ions, attributed solely to HNO_2, we can calculate the efficiency of the NO_2^- ion formation specifically from gaseous HNO_2.

Similar to the NO_2^- ion formation efficiency, we can define the transport efficiency for H_2O_2 and O_3. This is calculated as the ratio of the number of dissolved H_2O_2 (or O_3) molecules measured in the water after the experiment to the total number of H_2O_2 (or O_3) molecules present in the gas phase during the experiment.

Figure 7 shows the NO_2^- ion formation efficiencies from NO_2 and HNO_2, along with the transport efficiencies for O_3 (from 450 ppm O_3 in air) and H_2O_2 (from 100 ppm H_2O_2 in air), and the dimensionless Henry's law coefficients of the same species. The water volume in the compared experiments was 500 μl, and the treatment time was 1 min. By comparing the species shown in Fig. 7, we can see that the NO_2^- formation efficiency in water from HNO_2 is about 0.14 (i.e. 14% of the available HNO_2 molecules were dissolved in water) and this is about 23 times higher compared to the NO_2^- formation efficiency from NO_2.

An even higher transport efficiency was observed in experiments with H_2O_2, about 0.32 (32% of the available H_2O_2 molecules were dissolved in the water). Ozone, on the other hand, showed the lowest transport efficiency. These results are consistent with the low solubility of O_3 and the high solubility of H_2O_2, as predicted by the Henry's law constants of these species. The transport of H_2O_2 and O_3 to bulk water is described in more detail in our previous work [65]. However, we must emphasize that the ratios between the formation/transport efficiencies of individual species are not the same as the ratios of their Henry's law coefficients. Figure 7 also shows the dimensionless Henry's law coefficients k_H^{CC} of the studied species for easy comparison with their formation/transport efficiencies.

The variables on both vertical axes in Fig. 7 are dimensionless quantities and span over 8 orders of magnitude. On the scale shown, the values of both quantities for H_2O_2 are visually almost the same. This is not the case for NO_2, HNO_2, and O_3. Their values of the measured formation/transport efficiency are much larger than the value of their
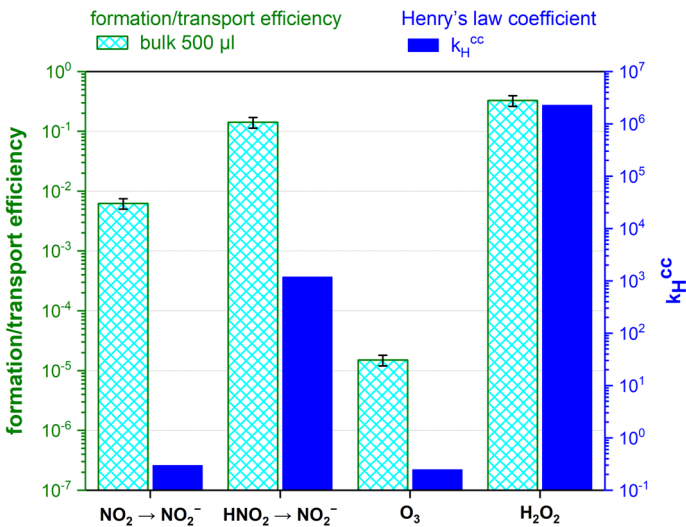

Fig. 7 Comparison of the formation efficiency of NO_2^- from NO_2 and from HNO_2, and the transport efficiency of O_3 and H_2O_2 with the dimensionless Henry's law coefficients (k_H^{cc}) of NO_2, HNO_2, O_3, and H_2O_2

dimensionless Henry's law coefficient. This means that NO_2, HNO_2, and O_3 are dissolved in our experiments with better efficiency than we would expect based only on their Henry's law solubility coefficients, or taken from the other end, H_2O_2 is dissolved less efficiently compared to the other three species.

It should be noted that the strong dissolution of H_2O_2 depleted it from the gas phase, as its concentration was only ~ 100 ppm [65]. If the depletion of H_2O_2 in the gas phase had not occurred, the amount of the transported H_2O_2 into water could have been even greater. Moreover, Henry's law coefficient describes the ratio of the concentrations of a given substance in a liquid and gas at equilibrium. In our 1–4 min experiments, equilibrium was probably not yet reached.

Figure 8 shows the decrease of the NO_2^- formation efficiency from gaseous NO_2 (250 ppm of NO_2 in the inlet gas) with the increasing treatment time, demonstrating that the steady-state conditions have not been reached. With increasing treatment time, the achieved concentration of NO_2^- in the liquid starts to play a role leading to a saturation effect. The decrease in NO_2^- formation efficiency is most pronounced at the smallest water volume of 200 μl, where the highest NO_2^- concentration is obtained. One reason for this saturation may be a gradual conversion of NO_2^- to NO_3^- in water, resulting in a pH decrease. This lower pH, in turn, further promotes the conversion of NO_2^- to NO_3^-, thereby diminishing the calculated NO_2^- formation efficiency.

Transport of species from external sources into water microdroplets

Figure 9a shows the amount of NO_2^- ions produced by dissolving NO_2 (from a mixture of synthetic air with 250 ppm of NO_2) and Fig. 9b shows the amount of NO_2^- ions produced by dissolving HNO_2 (from a $NO/NO_2/HNO_2$ mixture, NO_2 contribution subtracted, pure NO contribution negligible) in microdroplets from the nebulizer and electrospray. The water flow rate in the nebulizer experiments was 500 μl/min. In the ES experiment,
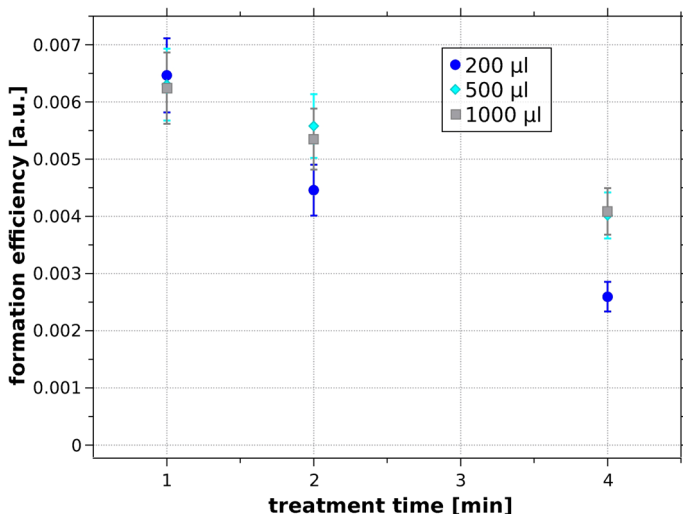

Fig. 8 Formation efficiency of NO_2^- ions from NO_2 gas as a function of treatment time and bulk water volume
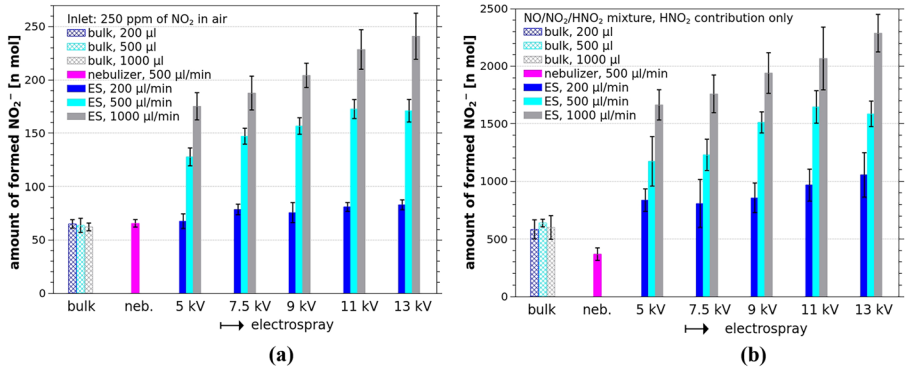
Fig. 9 Molar amount of NO_2^- ions formed in water in the experiment with **a** 250 ppm of NO_2 in the inlet gas, **b** $NO/NO_2/HNO_2$ mixture (NO_2 contribution subtracted); comparison of the amount of NO_2^- ions formed in the bulk water (1 min, water volume 200–1000 μl), in nebulized microdroplets (water flow rate 500 μl/min, half of the amount of NO_2^- formed in 4 min is shown) and in ES microdroplets (applied voltage 5–13 kV, water flow rate 200–1000 μl/min, 2 min)

the water flow rate was varied between 200 and 1000 μl/min, while the applied voltage ranged from 5 to 13 kV. The treatment time in the ES experiments was 2 min, whereas it was extended to 4 min in the nebulized microdroplets experiments due to insufficient water condensation in the ice bath within the initial 2-min period.

Figure 9 presents the estimated amount of NO_2^- ions formed in condensed water from the nebulizer within a 2-min timeframe. This estimate was derived by dividing the NO_2^- amount measured in the condensed water after 4 min by 2. For comparison, Fig. 9 also includes results from 1-min bulk water experiments (Figs. 5b and 6). We chose the 1-min bulk water data for this comparison because, in the flow-through microdroplet experiment, the average water residence time within the reactor is half of the total 2-min treatment time.

Similar data sets were previously obtained for the other molecules studied, O_3 and H_2O_2 [65] Fig. 10a shows the molar amount of O_3, and Fig. 10b the molar amount of H_2O_2
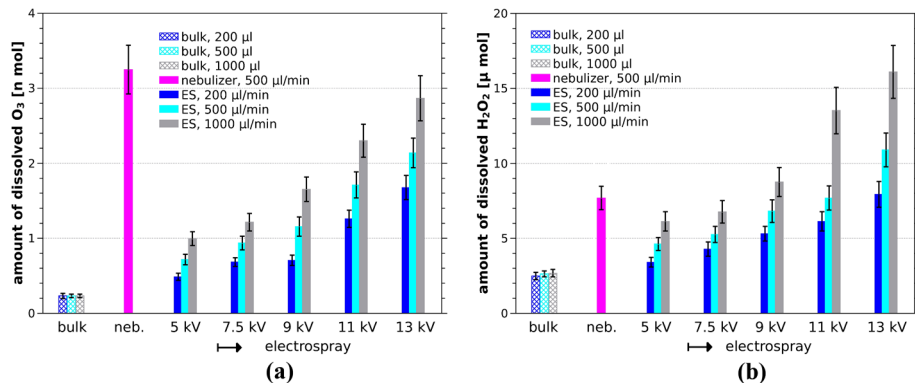

Fig. 10 Molar amount of (**a**) O_3 and (**b**) H_2O_2 dissolved in water, comparison of bulk water (1 min, water volume 200–1000 μl), nebulized microdroplets (water flow rate 500 μl/min, half of the amount of O_3/H_2O_2 transported in 4 min is shown) and ES microdroplets (applied voltage 5–13 kV, water flow rate 200–1000 μl/min, 2 min). Data were partly taken from [65]

transported to water microdroplets (and bulk water for comparison) here with added data for nebulized microdroplets. In all four data sets, there is the same trend regarding the amount of NO_2^- formed in and O_3/H_2O_2 transferred into ES microdroplets. We see not only the increase with the increasing applied voltage, but especially a significant increase with increasing water flow rate. For the flow rate of 1000 μl/min and the applied voltage of 13 kV, we obtained at least a fourfold enhancement for NO_2^- ions and H_2O_2 compared to the bulk water, and for O_3 even stronger.

The increase in the amount of NO_2^- ions formed in the ES microdroplets with the applied voltage and the water flow rate could be explained by the increasing total interface between the gas and water phases. As the applied voltage increases, the droplet size decreases, resulting in their larger surface area relative to the volume [65, 66]. As the water flow rate increases, there is a greater number of microdroplets. Figure 11a shows the total surface area of the gas–water interface for ES microdroplets as a function of the applied voltage and the water flow rate. For comparison, the surface area in the bulk water experiment and the nebulized microdroplets are also shown.

The bulk water area exposed to the gas species is only 130 mm^2 and is determined by the reactor size. In the case of nebulized microdroplets, we first calculated the total number of spherical monodisperse droplets with a diameter of 1 μm diameter produced from 1000 μl of water (flow rate 500 μl/min, experiment duration of 2 min). The total surface area of 6×10^6 mm^2 was then obtained by multiplying the number of microdroplets by the area of one microdroplet. We followed a similar procedure to calculate the total surface area for the ES microdroplets. However, the ES microdroplets are not uniform in diameter. For each applied voltage and water flow rate, we measured the number of droplets with different diameters (5–400 μm) [65, 66]. We used the obtained histograms of the polydisperse distribution of diameters to estimate the total gas–water surface area over the 2 min duration of the experiment, as shown in Fig. 11a.

Figure 11a shows the total surface area of microdroplets. If we consider the gas-to-water transport based on the surface area alone, we should obtain much better transport using ES microdroplets than in the bulk water experiment, and even several orders of magnitude better transport when using the smaller nebulized microdroplets. However, this was not
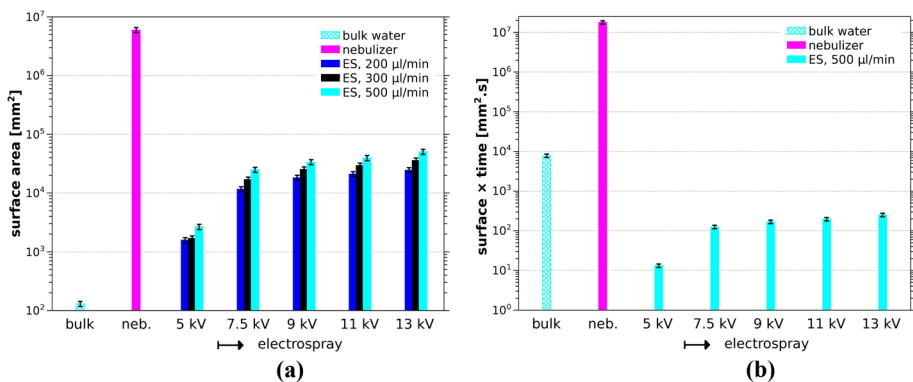

Fig. 11 **a** Total surface area of ES microdroplets as a function of the applied voltage, water flow rates 200–500 μl/min, and treatment time 2 min. Comparison with bulk water surface area and the total surface area of nebulized microdroplets (in 2 min, water flow rate of 500 μl/min); **b** product of water microdroplet surface area and the interaction time (60 s for bulk water, 3 s for nebulized microdroplets, 0.005 s for ES microdroplets), water flow rate of ES and nebulized microdroplets 500 μl/min

experimentally observed. Another key parameter to consider in the studied RONS transport is the gas–water interaction time. In the bulk water experiment, it is 60 s. For the nebulized microdroplets, it is the residence time of the carrier gas in the reactor. For the gas flow rate of 1 l/min and the given reactor volume (50 ml), the residence time of the gas in the nebulizer reactor is 3 s. For ES microdroplets, we define the interaction time as the average lifetime of the microdroplets, spanning from their formation at the nozzle to their impact on the reactor wall. With an average velocity of 5 m/s and an average traveled path of 2.5 cm, the average time of flight of an ES microdroplet through the reactor is as low as 0.005 s. Figure 11b compares the product of the gas–water interface surface area and the interaction time for bulk water, nebulized microdroplets, and ES microdroplets (water flow rate of 500 µl/min).

Compared to the interaction (i.e. treatment) time in the bulk experiment (on the order of 100 s), the lifetime of flying ES microdroplets is 4–5 orders of magnitude shorter. Considering that the product of the total surface area×treatment time of the ES microdroplets is less compared to the bulk due to their much shorter lifetime, one should actually expect a lower amount of dissolved RONS in the ES microdroplets than in the bulk water. However, this again contradicts the experimental results. To fully consider the interaction of RONS with water, it is necessary to consider a gradual formation of a bulk water at the bottom of the reactor during the ES experiments, where the total amount of dissolved RONS molecules is given by the sum of those dissolved during the short lifetime of the flying ES microdroplets and those dissolved in the bulk water formed at the bottom of the reactor, which stay there for much longer time.

It should be noted, however, that the absolute comparison of the results obtained in the bulk water experiments and the ES experiments is not straightforward. First, the surface area of the bulk water in the bulk reactor and in the ES reactor is different. Second, in the ES experiments, the water is sprayed into the reactor gradually, while in the bulk water batch experiments, water is in the reactor all the time from the beginning. The average time the water is exposed to the gaseous species in the ES experiment is only half the treatment time of the bulk experiment.

For this reason, the results of the ES experiments at 13 kV with a duration of 2 min and a water flow rate of 500 µl/min are compared with the data from the bulk water experiment with a duration of 1 min and a water volume of 1000 µl. In these two data sets, the average time during which the water is exposed to the gaseous species is the same, as well as the total volume of water treated. The same approach is used to compare data from the nebulized microdroplets and bulk water experiments.

Figure 12 shows on the left axis the NO_2^- ion formation efficiencies from NO_2 and HNO_2, along with the transport efficiencies for O_3 and H_2O_2, measured in the experiments with the nebulized microdroplets and ES microdroplets (at 13 kV), both with water flow rate of 500 µl/min and treatment time of 2 min, and bulk water volume of 500 µl and the treatment time of 1 min. The right axis shows the dimensionless Henry's law coefficients (k_H^{cc}) of the same species. This figure shows an addition of the nebulized and ES microdroplets to Fig. 7.

As shown previously in Fig. 7, the NO_2^- formation efficiency in bulk water from HNO_2 is about 0.14 (i.e. 14% of the available HNO_2 molecules were dissolved in water) and this is about 23 times higher compared to the NO_2^- formation efficiency from NO_2. There is a slight increase of the NO_2^- formation efficiency from NO_2 in the ES microdroplets compared to the bulk, while the nebulizer microdroplets decreased it compared to the bulk. A similar effect is visible for NO_2^- formation efficiency from HNO_2: the nebulizer microdroplets reduced the NO_2^- formation efficiency compared to the bulk, while the ES
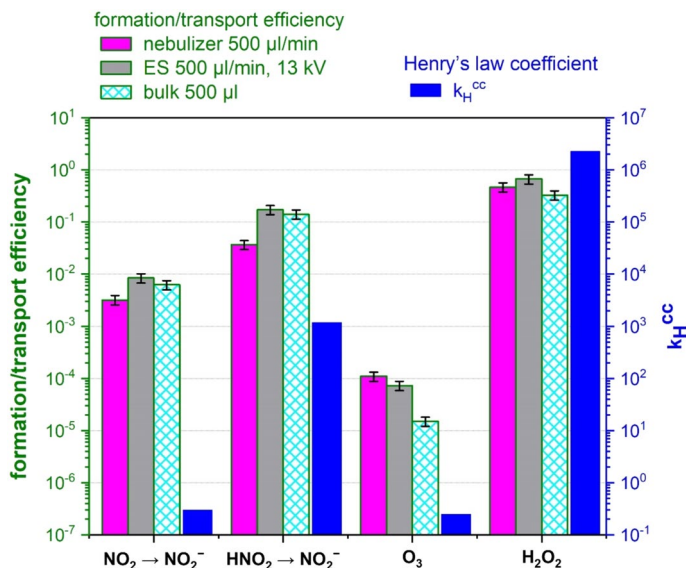
Fig. 12 Comparison of the formation efficiency of NO_2^- from NO_2 and from HNO_2, and the transport efficiency of O_3 and H_2O_2 in the nebulized microdroplets (2 min, 500 μl/min), ES microdroplets (13 kV, 2 min, 500 μl/min), and bulk water (1 min, 500 μl) with the dimensionless Henry's law coefficients ($k_H.^{cc}$) of NO_2, HNO_2, O_3, and H_2O_2

slightly increased it. The NO_2^- formation efficiency in the ES is about 5 times higher than in the nebulizer microdroplets.

The transport efficiency of H_2O_2, was slightly enhanced in both the nebulized and the ES microdroplets compared to the bulk water experiment, while the transport efficiency of O_3 was significantly enhanced in both the nebulized and the ES microdroplets up to 7 times. These results are consistent with the low solubility of O_3 and the high solubility of H_2O_2, as expected by Henry's law coefficients of these species, also shown in Fig. 12.

As discussed before with Fig. 7, NO_2, HNO_2, and O_3 are dissolved in the bulk experiments with much better efficiency than we would expect based only on their Henry's law solubility coefficients, and this effect is even enhanced by aerosolized microdroplets, most visibly for O_3.

Figure 13 displays the relative increase in the formation of NO_2^- ions from NO_2 or HNO_2, as well as the relative increase in the dissolved amounts of O_3 and H_2O_2, when comparing electrospray and nebulized microdroplets to the bulk water experiments. This relative increase was calculated by dividing the molar amount of a given species (NO_2^-, O_3, or H_2O_2) obtained in the microdroplet experiments by the molar amount of the same species obtained in the bulk water experiments.

Data in Fig. 13 confirm that transitioning from bulk water to microdroplets most significantly enhances ozone dissolution. This result was expected, considering ozone's low solubility, as evidenced by its low Henry's law coefficient and transport efficiency (Fig. 12). For ozone, the substantial increase in interaction surface area resulting from microdroplet formation seems to be the primary contributing factor.

The use of nebulized microdroplets is more suitable for the solvation of O_3, while the use of ES microdroplets is better for the formation of NO_2^- from NO_2 or HNO_2. We suggest that this phenomenon may be related to the fact that the ES microdroplets are electrically
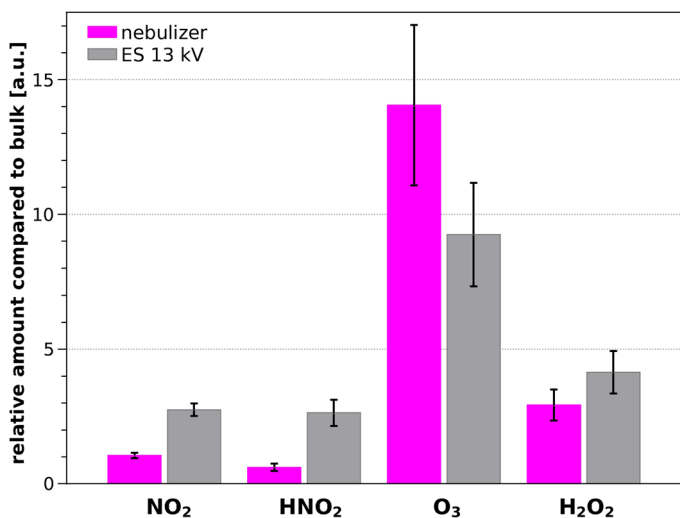
Fig. 13 Relative increase in the molar amount of NO_2^- ions formed from NO_2 or HNO_2, and the solvated O_3 and H_2O_2 in ES (13 kV, 2 min, 500 µl/min) and nebulized microdroplets (in 2 min, 500 µl/min) compared to the bulk water (1 min, 1000 µl)

positively charged, unlike the nebulized microdroplets. Detailed evaluation of the effect of the charge of the microdroplets on the solubility of different RONS will require further research. Here, we show that for the formation of NO_2^- from NO_2 and HNO_2, it is much more advantageous when using the charged ES than with the nebulized microdroplets, even though the nebulized microdroplets have a much larger surface area to volume ratio than the ES microdroplets.

Transport of reactive species from plasma discharge to water microdroplets

The electrical circuit shown in Fig. 4 can generate both self-pulsing streamer corona (SC) and transient spark (TS) discharges, depending on the external ballast resistor (R) used. The generation of TS typically requires an external ballast resistor of less than 10 MΩ. On the other hand, R above 20 MΩ is required to generate SC and avoid the formation of occasional spark pulses. By using $R = 13$ MΩ, it is possible to generate a mixed discharge regime, where both SC and TS coexist.

As shown in our previous research, both SC and TS are compatible with the simultaneous generation of water microdroplets by electrospray. Here, we verified that these two discharges can also operate with nebulized microdroplets. The electrical characteristics of the SC and TS current pulses with the ES microdroplets and with the nebulized microdroplets were not significantly different (Fig. 14 and Table 3). The repetition rate of the SC current pulses was slightly below 4 kHz, while the repetition rate of the TS current spark pulses was approximately 100 Hz (Table 3). Despite the presence of spark pulses, the total discharge power remained low, below 0.3 W, and the total input energy density was about 16 J/l, at an air flow rate of 1 l/min.

By utilizing a hybrid SC-TS discharge regime, we aimed to create a low-power plasma that combines the chemical reactivity of both SC and TS discharges. This
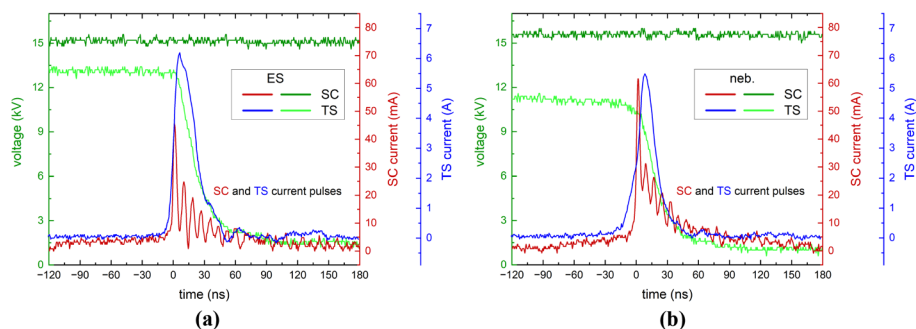
Fig. 14 Voltage and current waveforms of hybrid streamer corona—transient spark (SC-TS) discharge; **a** SC and TS with ES microdroplets; **b** SC and TS with nebulized microdroplets

Table 3 Electrical parameters of the hybrid streamer corona—transient spark discharge with ES or nebulized microdroplets at constant $Q_w = 500$ µl/min

	discharge	frequency (Hz)	power ± 0.005 (W)	energy density ± 0.3 (J/l)
ES	SC	3800 ± 20	0.134	8
	TS	76 ± 1	0.124	7.4
nebulizer	SC	3600 ± 30	0.141	8.5
	TS	107 ± 1	0.126	7.6

approach was expected to yield plasma-activated water (PAW) with a balanced concentration of ozone, hydrogen peroxide, and nitrite. Specifically, the SC discharge would predominantly generate ozone in humid air, while the TS discharge would primarily produce nitrogen oxides and nitrous acid, which could further react to form nitrite ions. Both discharges were expected to contribute to hydrogen peroxide formation.

Figure 15 shows (in logarithmic scale) the molar amounts of O_3, H_2O_2, and NO_2^- transported/formed in water by the hybrid SC-TS discharge. The treatment time in the ES experiments was 2 min. The treatment time in the nebulized microdroplets experiments was 4 min due to the need to accumulate minimal analyzable water volumes and the total molar amount of RONS transported/formed in the PAW was then divided by 2.

Using the ES microdroplets, the concentrations of RONS in water increased with increasing water flow rate. For the flow rate of 1000 µl/min, we obtained the largest amounts of O_3, H_2O_2, and NO_2^- ions.

When comparing the nebulizer and ES at 500 µl/min, slightly more H_2O_2 is transported from the plasma to the nebulized microdroplets than to the ES microdroplets. On the other hand, more NO_2^- ions are formed in ES microdroplets than in nebulized microdroplets. This finding agrees with the results of the previous section: for the formation of NO_2^-, it is much more advantageous to use the charged ES than the nebulized microdroplets.

The molar ratio of H_2O_2 to NO_2^- ions is smaller in ES microdroplets (approximately 2:1) than in nebulized microdroplets (approximately 6:1). The relatively balanced concentration of both H_2O_2 and NO_2^- in the formed PAW is an important factor in its antibacterial effects, as these two species largely determine the formation of the strongly antimicrobial peroxynitrite $ONOO^-$ [60].
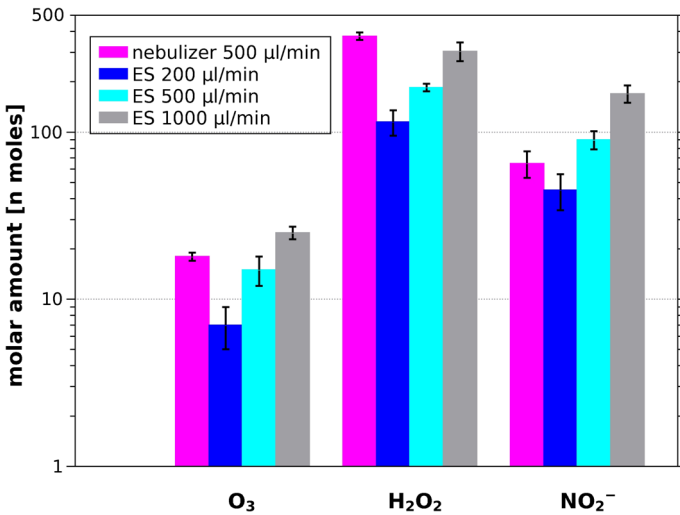
Fig. 15 Molar amounts of O_3, H_2O_2, and NO_2^- in PAW produced by hybrid SC-TS plasma after 2 min of treatment. The water flow rate from the nebulizer was 500 μl/min, for the ES microdroplets it varied in the range of 200 to 1000 μl/min

Figure 16 compares the molar amounts of O_3, H_2O_2, and NO_2^- transported into water produced using the hybrid SC-TS plasma interacting with nebulized microdroplets and ES microdroplets (at 13 kV), both with a water flow rate of 500 μl/min. Additionally, the amounts of O_3, H_2O_2, and NO_2^- transported into water in experiments with external sources of gas species are also shown, for both types of microdroplets at a water flow rate
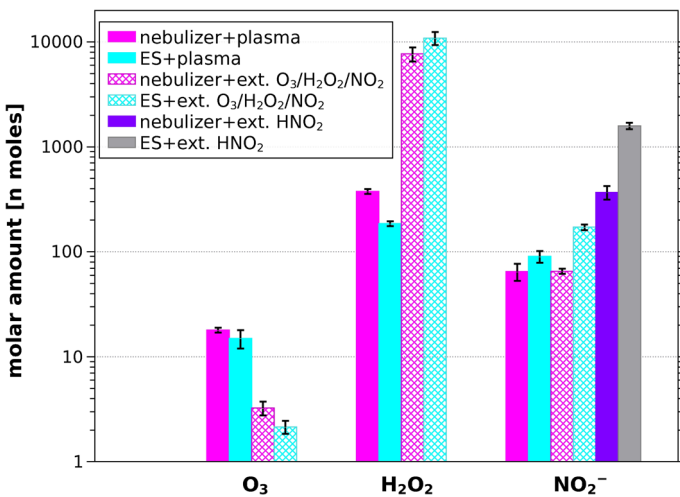
Fig. 16 Comparison of the molar amounts of O_3, H_2O_2, and NO_2^- formed in water by hybrid SC-TS plasma discharge (produced in 2 min, nebulized and ES microdroplets, $Q_w = 500$ μl/min), with the molar amounts obtained in experiments with RONS from the external sources (O_3 generator, H_2O_2 solution, 250 ppm NO_2 gas in air, and HNO_2 solution)

of 500 μl/min. For NO_2^-, the results are shown for the inlet air enriched either with NO_2 or with HNO_2.

Figure 16 shows (in logarithmic scale) that significantly more H_2O_2 is transported to microdroplets from the external source than from the SC-TS plasma. Assuming a linear relationship between H_2O_2 concentration in water and the gas phase, we can extrapolate that the inlet gas H_2O_2 concentration of the external source would need to be reduced from 100 ppm to 1–5 ppm to achieve roughly the same amount of H_2O_2 in water as observed in PAW from experiments with the SC-TS plasma (Fig. 17).

This can be also interpreted that the plasma generates gaseous H_2O_2 at a concentration of 1–5 ppm to achieve the observed molar amount of H_2O_2 in PAW. This concentration is below the detection limit of our electrochemical gas sensor. However, we cannot exclude the possibility that some H_2O_2 was generated directly in the liquid water through other pathways, such as from OH, HO_2, or $O(^1D)$ radicals [72–77]. Therefore, the actual concentration of H_2O_2 in air produced by SC-TS discharge may have been even lower than the estimated 1–5 ppm.

The amount of O_3 transported into water from SC-TS plasma was significantly higher than that from the external O_3 source (450 ppm). To match the amount of O_3 in PAW, the external O_3 source would require a concentration of 2000–3000 ppm (Fig. 17), assuming a linear relationship between O_3 concentration in water and gas. However, generating such a high concentration of O_3 with a hybrid SC-TS discharge is unlikely, especially given that TS does not generate ozone but rather NO due to a higher temperature in the discharge channel. It is more probable that the measured O_3 concentration in water from the plasma does not reflect the actual value, as the indigo blue reagent used in the spectrophotometric analysis is not perfectly selective for O_3. This reagent can also be oxidized by other oxidizing agents present in PAW [78].

Regarding NO_2^-, approximately the same amount was generated by the SC-TS plasma as in the water from the experiments with NO_2 from a pressure cylinder. To achieve similar
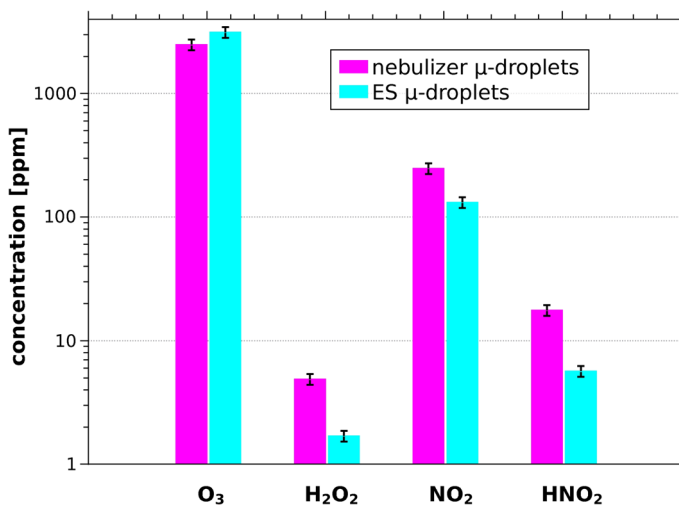

Fig. 17 Extrapolated concentrations of O_3, H_2O_2, NO_2, and HNO_2 that would have to be in the inlet gas in the experiments with external sources of these species, to achieve the same molar amounts of O_3, H_2O_2, and NO_2^- in the PAW generated by the hybrid SC-TS plasma discharge

NO_2^- concentrations in water using an external NO_2 gas source, the NO_2 gas concentration would have to be adjusted to 130 ppm (for ES microdroplets) or 260 ppm (for nebulized microdroplets). Based on our previous research results, generating 130–260 ppm of NO_2 in the plasma would require a significantly higher frequency of the TS current pulses (> 1 kHz) and significantly higher input energy density (> 100 J/l) [79].

Therefore, it is highly unlikely that the hybrid SC-TS discharge regime used in these experiments could generate enough NO_2 to account for the observed amount of NO_2^- in PAW. This suggests that even in the presence of plasma, NO_2 alone does not appear to be the dominant contributor to the formation of NO_2^- in PAW, but it is gaseous HNO_2.

Comparing the amount of NO_2^- produced in the experiment with an external HNO_2 source to that generated by plasma shows that 5–15 ppm of HNO_2 in the inlet gas would be sufficient to achieve the same level of NO_2^- in the water as observed with the plasma. Our previous research found that a TS discharge in air with ES microdroplets (100 μl/min) generated the HNO_2 concentration of approximately 25 ppm at the input energy density of about 120 J/l [63].

This suggests that it is theoretically plausible that the necessary amount of HNO_2, with an approximate 5 ppm concentration in air, has been produced in our experiment with hybrid SC-TS discharges. Therefore, we confirm in agreement with our previous findings [63] that HNO_2 plays a significant role in the formation of NO_2^- in PAW, not only when using TS but also with hybrid SC-TS discharges.

Conclusions

The transport of typical air plasma reactive oxygen and nitrogen species (RONS) into water was experimentally investigated, focusing on HNO_2, NO_2, and NO, as well as H_2O_2 and O_3, each with distinct Henry's law solubility coefficients. First, external sources of these single gaseous species were employed to compare their transport into bulk water versus water aerosols of charged electrosprayed (ES) or uncharged nebulized microdroplets. Second, the transport of these species generated in a mixture by a hybrid streamer-spark discharge in the air interacting with ES or nebulized microdroplets was investigated.

Comparing NO_2^- ion concentrations in water from experiments using NO and NO_2 cylinders, as well as a HyNOx gas mixture (approximately 600 ppm NO, 250 ppm NO_2, and 100 ppm HNO_2), revealed that NO's contribution to NO_2^- ion formation is negligible, while NO_2 contributes to about 10% of the formed NO_2^-. The primary contributor to NO_2^- ion formation is gaseous HNO_2.

When comparing the dimensionless Henry's law coefficients of NO_2, HNO_2, O_3, and H_2O_2 with the formation efficiency of NO_2^- from NO_2 or HNO_2, and the transport efficiencies of O_3 and H_2O_2, we observe a higher transport efficiency of O_3, and a much higher formation efficiency of NO_2^- from NO_2 or HNO_2 than predicted by Henry's law, compared to the transport efficiency of H_2O_2. The formation efficiency of NO_2^- ions from NO_2 decreases with treatment time, particularly for smaller volumes of bulk water, indicating a saturation effect of NO_2^- ions in water.

The improvement in transport/formation efficiencies by nebulized and ES microdroplets, where the surface area is significantly enhanced compared to the bulk water, is most evident for the weakly soluble O_3. For RNS, NO_2^- ion formation efficiency was strongly improved in ES microdroplets compared to bulk water, and this improvement increased with higher applied ES voltages. This is likely due to the charge effect in ES microdroplets, which

enhances the formation of aqueous nitrite NO_2^- ions when NO_2 or HNO_2 are transported into water. Further research is needed to fully understand the influence of microdroplet charge on the transport of different species from gas to liquid water.

Comparisons of the molar amounts of O_3, H_2O_2, and NO_2^- formed in water by hybrid SC-TS plasma discharge with those obtained with RONS from the external sources showed that.

1) significantly more H_2O_2 was transported to microdroplets from the external source than from the SC-TS plasma, indicating that the discharge likely produced as low as 1–5 ppm to achieve the measured aqueous concentration;

2) the amount of O_3 transported into water from SC-TS plasma was significantly higher than that from the external O_3 source: as high as 2000–3000 ppm of O_3 would be needed to match the amount of O_3 measured in PAW, which is unlikely, and may indicate non-specificity of the indigo blue chemical reagent used for aqueous O_3 concentration measurement;

3) HNO_2 with only 5–15 ppm concentration is the main gaseous precursor of NO_2^- in the water as observed by the hybrid SC-TS plasma discharge because the produced TS plasma has a relatively low frequency and low input energy density to produce a sufficient NO_2 to achieve the same amount of NO_2^- in the water.

The findings in this work contribute to a better understanding of the solvation process of typical long-lived air plasma-generated RONS. Knowledge of key solvation parameters, such as plasma-water surface area and microdroplet charge, can aid in producing plasma-activated water (PAW) more efficiently and selectively with respect to desired RONS composition. This will lead to the optimization of PAW generation plasma systems, which can be utilized for various applications in biomedicine, environment, and agriculture.

Declarations

Conflict of interest The authors declare no competing interests.

References

1. Bruggeman PJ, Kushner MJ, Locke BR et al (2016) Plasma–liquid interactions: a review and roadmap. Plasma Sources Sci Technol 25:053002. https://doi.org/10.1088/0963-0252/25/5/053002
2. Brisset JL, Pawlat J (2016) Chemical Effects of Air Plasma Species on Aqueous Solutes in Direct and Delayed Exposure Modes: Discharge, Post-discharge and Plasma Activated Water. Plasma Chem Plasma Process 36:355–381. https://doi.org/10.1007/S11090-015-9653-6
3. Ono R (2016) Optical diagnostics of reactive species in atmospheric-pressure nonthermal plasma. J Phys D Appl Phys 49:083001. https://doi.org/10.1088/0022-3727/49/8/083001
4. Schmidt-Bleker A, Bansemer R, Reuter S, Weltmann KD (2016) How to produce an NOx- instead of Ox-based chemistry with a cold atmospheric plasma jet. Plasma Processes Polym 13:1120–1127. https://doi.org/10.1002/PPAP.201600062
5. Atkinson R, Baulch DL, Cox RA et al (2009) evaluated kinetic and photochemical data for atmospheric chemistry: supplement III IUPAC subcommittee on gas kinetic data evaluation for atmospheric chemistry. J Phys Chem Ref Data. 18:881. https://doi.org/10.1063/1.555832
6. Lu X, Naidis GV, Laroussi M et al (2016) Reactive species in non-equilibrium atmospheric-pressure plasmas: Generation, transport, and biological effects. Phys Rep 630:1–84. https://doi.org/10.1016/J.PHYSREP.2016.03.003
7. Julák J, Hujacová A, Scholtz V et al (2018) Contribution to the Chemistry of Plasma-Activated Water. Plasma Phys Rep 44:125–136. https://doi.org/10.1134/S1063780X18010075
8. Hoeben WFLM, van Ooij PP, Schram DC et al (2019) On the Possibilities of Straightforward Characterization of Plasma Activated Water. Plasma Chem Plasma Process 39:597–626. https://doi.org/10.1007/S11090-019-09976-7/TABLES/6
9. Bruggeman PJ, Bogaerts A, Pouvesle JM et al (2021) Plasma–liquid interactions. J Appl Phys 130:200401. https://doi.org/10.1063/5.0078076
10. Oehmigen K, Hähnel M, Brandenburg R et al (2010) The Role of Acidification for Antimicrobial Activity of Atmospheric Pressure Plasma in Liquids. Plasma Processes Polym 7:250–257. https://doi.org/10.1002/ppap.200900077
11. Graves DB (2012) The emerging role of reactive oxygen and nitrogen species in redox biology and some implications for plasma applications to medicine and biology. J Phys D Appl Phys 45:263001. https://doi.org/10.1088/0022-3727/45/26/263001
12. Čech J, Šťahel P, Ráheľ J et al (2020) Mass Production of Plasma Activated Water: Case Studies of Its Biocidal Effect on Algae and Cyanobacteria. Water (Basel) 12:3167. https://doi.org/10.3390/w12113167
13. Mentheour R, Machala Z (2022) Coupled Antibacterial Effects of Plasma-Activated Water and Pulsed Electric Field. Front Phys 10:664. https://doi.org/10.3389/FPHY.2022.895813
14. Kovalova Z, Leroy M, Kirkpatrick MJ et al (2016) Corona discharges with water electrospray for Escherichia coli biofilm eradication on a surface. Bioelectrochemistry 112:91–99. https://doi.org/10.1016/j.bioelechem.2016.05.002
15. Barekzi N, Laroussi M (2013) Effects of Low Temperature Plasmas on Cancer Cells. Plasma Processes Polym 10:1039–1050. https://doi.org/10.1002/PPAP.201300083
16. Metelmann HR, Seebauer C, Miller V et al (2018) Clinical experience with cold plasma in the treatment of locally advanced head and neck cancer. Clin Plasma Med 9:6–13. https://doi.org/10.1016/J.CPME.2017.09.001
17. Sersenová D, Machala Z, Repiská V, Gbelcová H (2021) Selective Apoptotic Effect of Plasma Activated Liquids on Human Cancer Cell Lines. Molecules 4254(26):4254. https://doi.org/10.3390/MOLECULES26144254
18. Naumova IK, Maksimov AI, Khlyustova AV (2011) Stimulation of the germinability of seeds and germ growth under treatment with plasma-activated water. Surf Eng Appl Electrochem 47:263–265. https://doi.org/10.3103/S1068375511030136
19. Kučerová K, Henselová M, Slováková Ľ, Hensel K (2019) Effects of plasma activated water on wheat: Germination, growth parameters, photosynthetic pigments, soluble protein content, and antioxidant enzymes activity. Plasma Processes Polym 16:1800131. https://doi.org/10.1002/PPAP.201800131
20. Maniruzzaman M, Sinclair AJ, Cahill DM et al (2017) Nitrate and Hydrogen Peroxide Generated in Water by Electrical Discharges Stimulate Wheat Seedling Growth. Plasma Chem Plasma Process 37:1393–1404. https://doi.org/10.1007/S11090-017-9827-5
21. Takaki K, Takahata J, Watanabe S et al (2013) Improvements in plant growth rate using underwater discharge. J Phys Conf Ser 418:012140. https://doi.org/10.1088/1742-6596/418/1/012140

22. Medvecká V, Omasta S, Klas M et al (2021) Plasma activated water prepared by different plasma sources: physicochemical properties and decontamination effect on lentils sprouts. Plasma Sci Technol 24:015503. https://doi.org/10.1088/2058-6272/AC3410
23. Guo J, Huang K, Wang X et al (2017) Inactivation of Yeast on Grapes by Plasma-Activated Water and Its Effects on Quality Attributes. J Food Prot 80:225–230. https://doi.org/10.4315/0362-028X.JFP-16-116
24. Perez SM, Biondi E, Laurita R et al (2019) Plasma activated water as resistance inducer against bacterial leaf spot of tomato. PLoS ONE 14:e0217788. https://doi.org/10.1371/JOURNAL.PONE.0217788
25. Tan J, Karwe MV (2021) Inactivation and removal of Enterobacter aerogenes biofilm in a model piping system using plasma-activated water (PAW). Innov Food Sci Emerg Technol 69:102664. https://doi.org/10.1016/J.IFSET.2021.102664
26. Tizaoui C, Ni Y (2017) Advanced oxidation processes and non-thermal plasma for the removal of emerging contaminants in water. In: 11th European Waste Water Management Conference 3rd – 4th October 2017, Leeds, UK
27. Brisset JL, Moussa D, Doubla A et al (2008) Chemical Reactivity of Discharges and Temporal Post-Discharges in Plasma Treatment of Aqueous Media: Examples of Gliding Discharge Treated Solutions. Ind Eng Chem Res 47:5761–5781. https://doi.org/10.1021/IE701759Y
28. Park DP, Davis K, Gilani S et al (2013) Reactive nitrogen species produced in water by non-equilibrium plasma increase plant growth rate and nutritional yield. Curr Appl Phys 13:S19–S29. https://doi.org/10.1016/J.CAP.2012.12.019
29. Lu P, Boehm D, Bourke P, Cullen PJ (2017) Achieving reactive species specificity within plasma-activated water through selective generation using air spark and glow discharges. Plasma Processes Polym 14:1600207. https://doi.org/10.1002/PPAP.201600207
30. Ng SW, Slikboer E, Dickenson A et al (2021) Characterization of an atmospheric pressure air plasma device under different modes of operation and their impact on the liquid chemistry. J Appl Phys 129:123303. https://doi.org/10.1063/5.0039171
31. Wartel M, Faubert F, Dirlau ID et al (2021) Analysis of plasma activated water by gliding arc at atmospheric pressure: Effect of the chemical composition of water on the activation. J Appl Phys 129:233301. https://doi.org/10.1063/5.0040035
32. Jõgi I, Talviste R, Raud S et al (2020) Comparison of two cold atmospheric pressure plasma jet configurations in argon. Contrib Plasma Phys 60:e201900127. https://doi.org/10.1002/CTPP.201900127
33. Uchida G, Nakajima A, Ito T et al (2016) Effects of nonthermal plasma jet irradiation on the selective production of H2O2 and NO2− in liquid water. J Appl Phys 120:203302. https://doi.org/10.1063/1.4968568
34. Vlad IE, Anghel SD (2017) Time stability of water activated by different on-liquid atmospheric pressure plasmas. J Electrostat 87:284–292. https://doi.org/10.1016/J.ELSTAT.2017.06.002
35. Anderson CE, Cha NR, Lindsay AD et al (2016) The role of interfacial reactions in determining plasma-liquid chemistry. Plasma Chem Plasma Process 36:1393–1415. https://doi.org/10.1007/S11090-016-9742-1
36. Bradu C, Kutasi K, Magureanu M et al (2020) Reactive nitrogen species in plasma-activated water: generation, chemistry and application in agriculture. J Phys D Appl Phys 53:223001. https://doi.org/10.1088/1361-6463/AB795A
37. Gorbanev Y, Privat-Maldonado A, Bogaerts A (2018) Analysis of short-lived reactive species in plasma-air-water systems: the dos and the do nots. Anal Chem 90:13151–13158. https://doi.org/10.1021/acs.analchem.8b03336
38. Khlyustova A, Labay C, Machala Z et al (2019) Important parameters in plasma jets for the production of RONS in liquids for plasma medicine: a brief review. Frontiers Chem Sci Eng 13:238–252. https://doi.org/10.1007/S11705-019-1801-8
39. Goldstein S, Lind J, Merényi G (2005) Chemistry of peroxynitrites as compared to peroxynitrates. Chem Rev 105:2457–2470. https://doi.org/10.1021/CR0307087/ASSET/CR0307087.FP.PNG_V03
40. OstrikovZhouZhou KKRR et al (2020) Plasma-activated water: generation, origin of reactive species and biological applications. J Phys D Appl Phys 53:303001. https://doi.org/10.1088/1361-6463/AB81CF
41. Raud S, Raud J, Jõgi I et al (2021) The Production of Plasma Activated Water in Controlled Ambient Gases and its Impact on Cancer Cell Viability. Plasma Chem Plasma Process 41:1381–1395. https://doi.org/10.1007/S11090-021-10183-6
42. Pavlovich MJ, Ono T, Galleher C et al (2014) Air spark-like plasma source for antimicrobial NOx generation. J Phys D Appl Phys 47:505202. https://doi.org/10.1088/0022-3727/47/50/505202

43. Sander R (1999) Compilation of Henry's Law Constants for Inorganic and Organic Species of Potential Importance in Environmental Chemistry, Version 3
44. Sander R (2015) Compilation of Henry's law coefficients (version 4.0) for water as solvent. Atmos Chem Phys 15:4399–4981. https://doi.org/10.5194/acp-15-4399-2015
45. Mai-Prochnow A, Zhou R, Zhang T, et al. (2021) Interactions of plasma-activated water with biofilms: inactivation dispersal effects and mechanisms of action. npj Biofilms and Microbiomes. 7 1
46. Bruggeman P, Leys C (2009) Non-thermal plasmas in and in contact with liquids. J Phys D Appl Phys 42:053001. https://doi.org/10.1088/0022-3727/42/5/053001
47. Samukawa S, Hori M, Rauf S et al (2012) The 2012 Plasma Roadmap. J Phys D Appl Phys 45:253001. https://doi.org/10.1088/0022-3727/45/25/253001
48. Vanraes P, Nikiforov AY, Leys C (2016) Electrical Discharge in Water Treatment Technology for Micropollutant Decomposition. In: Plasma Science and Technology - Progress in Physical States and Chemical Reactions. InTech
49. Kruszelnicki J, Lietz AM, Kushner MJ (2019) Atmospheric pressure plasma activation of water droplets. J Phys D Appl Phys 52:355207. https://doi.org/10.1088/1361-6463/AB25DC
50. Silsby JA, Simon S, Walsh JL, Hasan MI (2021) The Influence of Gas-Liquid Interfacial Transport Theory on Numerical Modelling of Plasma Activation of Water. Plasma Chem Plasma Process 41:1363–1380. https://doi.org/10.1007/S11090-021-10182-7
51. Keniley S, Uner NB, Perez E et al (2022) Multiphase modeling of the DC plasma–water interface: application to hydrogen peroxide generation with experimental validation. Plasma Sources Sci Technol 31:075001. https://doi.org/10.1088/1361-6595/AC7891
52. Gorbanev Y, O'Connell D, Chechik V (2016) Non-Thermal Plasma in Contact with Water: The Origin of Species. Chem Eur J 22:3496–3505. https://doi.org/10.1002/chem.201503771
53. Winter J, Tresp H, Hammer MU et al (2014) Tracking plasma generated H2O2 from gas into liquid phase and revealing its dominant impact on human skin cells. J Phys D Appl Phys 47:285401. https://doi.org/10.1088/0022-3727/47/28/285401
54. Oinuma G, Nayak G, Du Y, Bruggeman PJ (2020) Controlled plasma-droplet interactions: A quantitative study of OH transfer in plasma-liquid interaction. Plasma Sources Sci Technol 29:095002. https://doi.org/10.1088/1361-6595/aba988
55. Machala Z, Tarabová B, Sersenová D et al (2019) Chemical and antibacterial effects of plasma activated water: Correlation with gaseous and aqueous reactive oxygen and nitrogen species, plasma sources and air flow conditions. J Phys D Appl Phys 52:034002. https://doi.org/10.1088/1361-6463/aae807
56. Janda M, Martišovitš V, Machala Z (2011) Transient spark: a dc-driven repetitively pulsed discharge and its control by electric circuit parameters. Plasma Sources Sci Technol 20:035015. https://doi.org/10.1088/0963-0252/20/3/035015
57. Sremački I, Bruno G, Jablonowski H et al (2021) Influence of aerosol injection on the liquid chemistry induced by an RF argon plasma jet. Plasma Sources Sci Technol 30:095018. https://doi.org/10.1088/1361-6595/ABE176
58. Burlica R, Grim RG, Shih K-Y et al (2010) Bacteria Inactivation Using Low Power Pulsed Gliding Arc Discharges with Water Spray. Plasma Processes Polym 7:640–649. https://doi.org/10.1002/ppap.200900183
59. Pyrgiotakis G, McDevitt J, Bordini A et al (2014) A chemical free, nanotechnology-based method for airborne bacterial inactivation using engineered water nanostructures. Environ Sci Nano 1:15–26. https://doi.org/10.1039/c3en00007a
60. Machala Z, Tarabova B, Hensel K et al (2013) Formation of ROS and RNS in Water Electro-Sprayed through Transient Spark Discharge in Air and their Bactericidal Effects. Plasma Processes Polym 10:649–659. https://doi.org/10.1002/ppap.201200113
61. Ogunyinka O, Wright A, Bolognesi G et al (2020) An integrated microfluidic chip for generation and transfer of reactive species using gas plasma. Microfluid Nanofluidics 24:1–16. https://doi.org/10.1007/S10404-019-2316-9
62. Liu Z, Wang S, Pang B et al (2021) The impact of surface-to-volume ratio on the plasma activated water characteristics and its anticancer effect. J Phys D Appl Phys 54:215203. https://doi.org/10.1088/1361-6463/ABE78F
63. Janda M, Hensel K, Tóth P et al (2021) The Role of HNO2 in the Generation of Plasma-Activated Water by Air Transient Spark Discharge. Appl Sci 11:7053. https://doi.org/10.3390/APP11157053
64. Stancampiano A, Gallingani T, Gherardi M et al (2019) Plasma and Aerosols: Challenges, Opportunities and Perspectives. Appl Sci 9:3861. https://doi.org/10.3390/app9183861
65. Hassan ME, Janda M, Machala Z (2021) Transport of Gaseous Hydrogen Peroxide and Ozone into Bulk Water vs. Electrosprayed Aerosol Water (Basel) 13:182. https://doi.org/10.3390/w13020182

66. Janda M, Hassan ME, Martišovitš V et al (2021) In situ monitoring of electrosprayed water micro-droplets using laser and LED light attenuation technique: Comparison with ultra-high-speed camera imaging. J Appl Phys 129:183305. https://doi.org/10.1063/5.0046593
67. Tachibana K, Nakamura T (2019) Comparative study of discharge schemes for production rates and ratios of reactive oxygen and nitrogen species in plasma activated water. J Phys D Appl Phys 52:385202. https://doi.org/10.1088/1361-6463/AB2529
68. Keller-Rudek H, Moortgat GK, Sander R, Sörensen R (2013) The MPI-Mainz UV/VIS spectral atlas of gaseous molecules of atmospheric interest. Earth Syst Sci Data 5:365–373. https://doi.org/10.5194/ESSD-5-365-2013
69. Eisenberg GM (1943) Colorimetric determination of hydrogen peroxide. Ind Eng Chem-Analyt Edit 15:327–328. https://doi.org/10.1021/i560117a011
70. Lukes P, Dolezalova E, Sisrova I, Clupek M (2014) Aqueous-phase chemistry and bactericidal effects from an air discharge plasma in contact with water: Evidence for the formation of peroxynitrite through a pseudo-second-order post-discharge reaction of H_2O_2 and HNO_2. Plasma Sources Sci Technol 23:015019. https://doi.org/10.1088/0963-0252/23/1/015019
71. Baird R, Rice EW, Eaton AD, et al (2017) Standard Methods for the Examination of Water and Wastewater, 23rd ed. American Public Health Association
72. Kanazawa S, Kawano H, Watanabe S et al (2011) Observation of OH radicals produced by pulsed discharges on the surface of a liquid. Plasma Sources Sci Technol 20:034010. https://doi.org/10.1088/0963-0252/20/3/034010
73. Bruggeman P, Schram DC (2010) On OH production in water containing atmospheric pressure plasmas. Plasma Sources Sci Technol 19:045025. https://doi.org/10.1088/0963-0252/19/4/045025
74. Zhou XF, Zhao ZL, Liang JP et al (2019) Measurement of reactive species in different solutions of bubble discharge with varying O2/N 2 proportion in Ar: Analysis of reaction pathways. Plasma Processes Polym 16:e1900001. https://doi.org/10.1002/PPAP.201900001
75. Locke BR, Shih KY (2011) Review of the methods to form hydrogen peroxide in electrical discharge plasma with liquid water. Plasma Sources Sci Technol 20:034006
76. Taube H (1957) Photochemical reactions of ozone in solution. Trans Faraday Soc 53:656–665. https://doi.org/10.1039/TF9575300656
77. Xu S, Jirasek V, Lukes P (2020) Molecular dynamics simulations of singlet oxygen atoms reactions with water leading to hydrogen peroxide. J Phys D Appl Phys 53:275204. https://doi.org/10.1088/1361-6463/AB8321
78. Tarabová B, Lukeš P, Janda M et al (2018) Specificity of detection methods of nitrites and ozone in aqueous solutions activated by air plasma. Plasma Processes Polym 15:1800030. https://doi.org/10.1002/ppap.201800030
79. Janda M, Hensel K, Machala Z, Field TA (2023) The influence of electric circuit parameters on NOx generation by transient spark discharge. J Phys D Appl Phys 56:485202. https://doi.org/10.1088/1361-6463/ACE634

Authors and Affiliations

Mostafa Elsayed Hassan[1,2,3] · Mário Janda[1] · Zdenko Machala[1]

✉ Mostafa Elsayed Hassan
   mostafa.hassan@fmph.uniba.sk

✉ Zdenko Machala
   machala@fmph.uniba.sk

   Mário Janda
   mario.janda@fmph.uniba.sk

[1]   Division of Environmental Physics, Faculty of Mathematics, Physics and Informatics, Comenius University, Mlynská Dolina, 842 48 Bratislava, Slovakia

[2]   Department of Physics, Faculty of Science, Ain Shams University, 11566 Cairo, Egypt

[3]   AG Experimentelle Plasmaphysik, Universität Augsburg, 86135 Augsburg, Germany